Thomas O. Meyer[1]
Department of Mechanical and Mechatronic Engineering,
Stellenbosch University,
Stellenbosch, Western Cape 7599, South Africa
e-mail: t.meyer23@gmail.com

Sybrand J. van der Spuy
Department of Mechanical and Mechatronic Engineering,
Stellenbosch University,
Stellenbosch, Western Cape 7599, South Africa
e-mail: sjvdspuy@sun.ac.za

Christiaan J. Meyer
Department of Mechanical and Mechatronic Engineering,
Stellenbosch University,
Stellenbosch, Western Cape 7599, South Africa
e-mail: cjmeyer@sun.ac.za

Alessandro Corsini
Dipartimento di Meccanica e Aeronautica,
Universitádi Roma "La Sapienza",
00185 Rome, Italy
e-mail: alessandro.corsini@uniroma1.it

Design of a Tip Appendage for the Control of Tip Leakage Vortices in Axial Flow Fans

This article reports on numerical investigations of passive control techniques used for the performance enhancement of a large diameter axial flow cooling fan through modification of the blade tip geometry. Using open-source software, a novel meshing strategy is developed to carry out both steady and unsteady numerical computations of a periodic section of an axial flow fan. Analyzing the flow near the blade tip with a reduction in tip clearance, two predominant flow phenomena are identified. These two flow phenomena are further investigated with the aim of controlling them through implementation of a tip appendage design. Both introduced end-plate designs indicate effective control of each relevant flow phenomena. The constant thickness (CT) end-plate design is found to increase all fan performance characteristics at lower than design point (DP) flowrates, while increasing the fan's peak efficiency plateau toward the rotor stall margin. However, none of the CT end-plate designs are able to improve the fan's performance characteristics at its DP. The introduction of a novel trailing-edge (TE) end-plate design is found to increase all fan performance characteristics across the entire evaluated stable operating range, with an indicated increase of 37.3 percent in total-to-static pressure rise and a 2.9 percentage point increase in total-to-static efficiency at the fan's DP flowrate. The aerodynamic performance results attest to the associated benefits of the investigated passive control techniques.
[DOI: 10.1115/1.4050359]

Keywords: passive control devices, tip end-plates, design optimization

Introduction

Air-cooled heat exchangers (ACHEs) find extensive application throughout the oil and gas industry as they minimize water consumption and provide for a cost-effective alternative over competing technologies. These types of heat exchangers make use of large industrial axial flow fans to affect the movement of large volumes of air over a multitude of heat exchanger bundles for cooling of the working fluid. As the fans consume relatively large amounts of electricity, a small improvement in the fan efficiency may lead to a significant saving in energy.

From 2016 to 2018, the European Union funded the MinWaterCSP project, which forms part of the larger Horizon 2020 research and innovation program. This project was aimed at reducing water usage in concentrated solar power plants while maintaining cycle efficiency. As part of the project scope, the M-Fan [1] was produced. The M-Fan is a rotor only axial flow fan designed for use in ACHEs. However, during scale experimental testing, the M-Fan could not meet the required design specifications as set out by the project. A possible cause for this could be related to tip clearance effects [2].

The flow near the blade tip is characterized by multiple complex and unsteady three-dimensional flow structures. The development of these flow structures is a result of the tip clearance that exists between the rotating blade tip and the stationary fan casing. A high blade loading present near the blade tip induces a localized flow, known as tip leakage flow (TLF), which flows from the high-pressure side (PS) to the low-pressure side of the blade. The skewed merging of this localized flow with the main flow motivates the formation of a tip leakage vortex (TLV) on the blade suction side (SS). The TLF, and subsequent TLV formation, is associated with having a detrimental effect on both fan pressure rise and fan efficiency [3].

Two predominant methods are employed within turbomachinery to mitigate the deleterious effects of TLF, namely, active and passive control techniques. The former makes use of dynamic means such as wall casing treatments and fluid injection to alter the interacting flow and thereby improve performance. However, the adoption of dynamic control devices has an inherent difficulty in identifying the characteristic frequencies of the vortical structures for the positional adjustment and intensity of such devices [4]. The second approach makes use of static means such as changes in blade configuration [5] or tip modification techniques [6–8] to achieve the same desired outcome. More recently, Corsini et al. [9–12] investigated the effect of locally thickening the blade tip based on a safe chord-wise Rossby number distribution on a family of commercially available axial flow fans. The findings indicated improved fan performance and aero-acoustic characteristics with an increased peak efficiency plateau toward the rotor stall margin.

This article is organized as follows. A description of the relevant test fan and numerical setup is initially given. Thereafter, a numerical investigation into tip clearance effects on fan performance characteristics is conducted to gain insight into the relevant flow phenomena present near the blade tip. Once identified, these flow phenomena are exploited to develop a tip appendage design methodology for the control of such phenomena with the aim of fan performance enhancement.

Methodology

Test Fan. The M-Fan was specifically developed for use in low pressure rise ACHE applications and as such has been both numerically and experimentally tested at model scale. It should be mentioned that the fan scaling laws do not take Reynolds number effects into account. Although the chord-based Reynolds number at the tip of the design fan is 4.78 times larger than that of the scale fan, the Reynolds numbers for both fans are in the fully

[1]Corresponding author.

Contributed by the International Gas Turbine Institute (IGTI) of ASME for publication in the Journal of Turbomachinery. Manuscript received November 11, 2020; final manuscript received January 12, 2021; published online April 9, 2021. Tech. Editor: David G. Bogard.

turbulent region. This means that the viscous effects stemming from the two fans would be similar. Table 1 presents the design specifications of the design and scale fan.

Meshing Strategy. In a comparative study involving various open-source meshing alternatives, a hybrid hexahedral dominant meshing strategy was developed by considering the various software packages capabilities. The meshing procedure is briefly described.

Stage 1: Base mesh creation. CFMESH v1.2 is used to initiate the meshing procedure through base mesh creation. Given an input stereolithography file and the required user-defined region refinements, an initial mesh is created, which minimizes nonorthogonality near surface patches. Edge refinement is divided into leading, trailing, and tip edges. The trailing edge (TE) is split 10 mm above the hub surface to allow for a coarser refinement to ensure proper layer growth in the later meshing stages.

Stage 2: Base mesh preparation. The built-in OPENFOAM function *refineWallLayer* is used in preparing the base mesh for later layer addition. The first cell row aligning surface patches that require layer addition are split multiple times using a set of predefined refinement factors. This is done to allow a smooth transfer of information between cells by limiting the maximum volume ratio between the added layer cells and the base mesh's internal cells. Care should be taken during this stage as the refinement function does not take the mesh quality into account. This means that a mesh of unacceptable quality can be easily generated.

Stage 3: Layer addition. The final stage makes use of OPENFOAM's snappyHexMesh layer addition phase. By switching off all mesh quality controls and carefully selecting the layer addition settings, to maximize growth, the layers are added to the specified patches. Although this method leads to the complete layer growth, the final mesh quality is highly dependent on the chosen total layer thickness and the local refinement level. These two meshing parameters are inversely proportional to acceptable mesh quality. If the total layer thickness is too large for a high level of refinement, the cells become highly warped and produce an unacceptable mesh quality.

The hub layers are added first to limit the deformation of the cells immediately surrounding the blade. The layer addition process is split into two addition phases: outer layer addition and near-wall layer addition. The outer layers are desired to have a higher expansion ratio to limit the maximum volume ratio between the added cells and the internal mesh. The near-wall layers are desired to have a lower expansion ratio, with the total added layers being in the range of 5–10. By using the *nMedialAxisIter* setting in snappyHexMesh, which limits cell deformation away from surface patches, the number of cells that become deformed can be controlled (to some degree), and therefore, a better mesh quality is achievable. All these settings are adjusted to optimize the number of layers and overall mesh quality.

Table 1 M-Fan design specifications

Specification	Design	Scale
Number of blades	8	8
Blade root stagger angle (°)	34	34
Fan rotor diameter D_F (m)	7.3152	1.53
Hub-to-tip diameter ratio (–)	0.29	0.29
Rotor tip clearance ratio (τ/D_F)	0.004	0.004
Blade tip angle of attack (deg)	0.685	–
Blade tip chord length l_c (m)	0.825	0.173
Volumetric flowrate (m^3/s)	333	14.57
Rotational speed (rpm)	151	722

The blade and casing layers are added in a similar manner to the hub. Since there is a tip gap between the blade tip and casing, these layers have to be added simultaneously to ensure that their respective growths do not interfere with each other. Noting this, it becomes apparent that the layers within the tip region have a tendency to become deformed as they grow in opposing directions. The *nMedialAxisIter* setting is again used here to limit this deformation and produce an acceptable mesh quality.

Domain Construction and Boundary Conditions. The computational domain consists of a 1/8th periodic section with extended hub and casing lengths to form the annular blade passage. A representation of the computational mesh with its specified patch names is shown in Fig. 1.

The mesh is constructed using the previously mentioned meshing strategy with the average y^+ value being in the range of $1 < y^+ < 5$ along the first node row of wall boundaries. This is done to facilitate the use of a low Reynolds approach.

A mesh convergence study was performed using a zero tip clearance as presented in Table 2. In this study, it was concluded that mesh 4 provided the best compromise between accuracy and size. In addition, an inlet and outlet patch displacement length of 1.25 m and 0.61 m from leading and trailing edges, respectively, provided for a converged solution. A node distribution of 16%, 74%, and 10% for the inlet, rotor, and outlet sections, respectively, was found to provided adequate domain resolution. Finally, with the design tip clearance introduced, a minimum mesh density requirement of 11.8×10^6 cells with at least 27 elements within the tip gap is found to complete the convergence study. Figure 2 shows the turbulence kinetic energy and final computational mesh at the blade tip for a 6 mm tip clearance.

A fixed uniform velocity profile is imposed on the inlet patch. Turbulence kinetic energy, k, is calculated using a turbulence intensity of 1% as this was determined to be the relevant case for the test facility at Stellenbosch University [13]. The specific rate of dissipation, ω, is based on a mixing length scale, l_{mix}, of 50% of the annulus height (blade span) as recommended by OpenCFD Ltd. [14]. All wall boundaries are imposed with a *no slip* velocity condition with all turbulence parameters being set to a fixed value less than that of the simulations' specified writing precision. Periodicity is specified to be upstream and downstream of the blade, while a Neumann condition is imposed on all outlet boundary fields. The blade, hub, and internal mesh are set to rotate at an angular speed equal to that specified in Table 1, while the remainder of the boundary patches is fixed to a stationary reference frame.

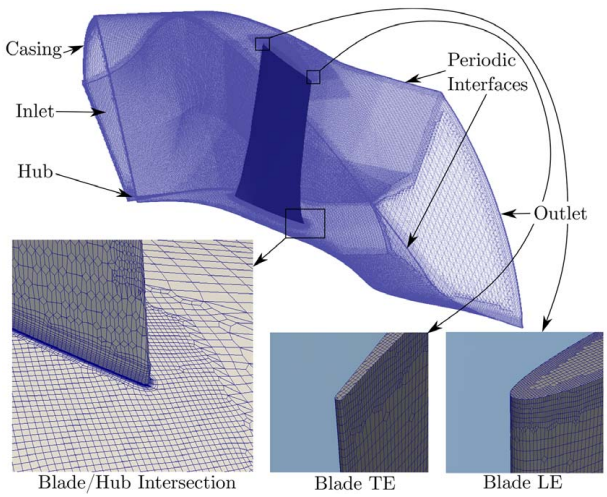

Fig. 1 Computational mesh

Table 2 Mesh density sensitivity of the scale M-Fan domain at the 14.68 m^3/s calculated DP flowrate of Wilkinson et al. [2] for a 0 mm tip clearance

Mesh	Cell count	ΔP_{t-s} (Pa)	η_{t-s} (−)	Refinement bias
1	4.1×10^6	96.07	0.529	Datum
2	7.4×10^6	91.70	0.514	RR
3	8.9×10^6	96.39	0.530	MCS
4	10.8×10^6	91.28	0.513	Mesh 2 + AMI
5	13.3×10^6	90.77	0.513	Mesh 4 + Mesh 3
6	13.7×10^6	90.39	0.511	Mesh 5 + RR

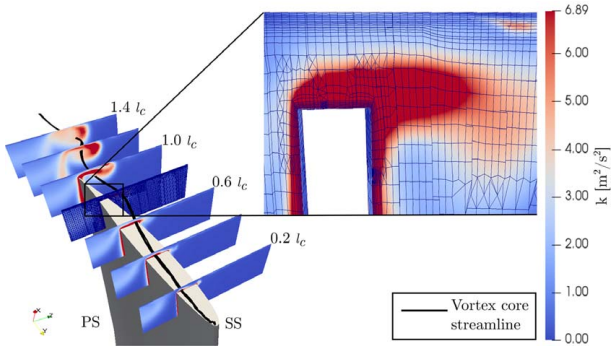

Fig. 2 Turbulence kinetic energy and computational mesh at blade tip for a 6 mm tip clearance at the fan's 14.57 m^3/s design point (DP) flowrate

Numerical Method. The Reynolds-averaged Navier–Stokes equations are solved in the rotating reference frame as they are considered an effective investigation tool for vortical structure detection [15]. As shown in Table 3, a turbulence model comparative study was performed using three turbulence models referenced in literature. The linear $k-\omega$ shear stress transport (SST) model of Menter et al. [16] is used to compute the turbulence transport equations as it is found to best predict fan performance when compared to the experimental data. This model requires no near-wall corrections, which accommodates solving through the wall boundary layer using a low Reynolds approach.

Solver Settings and Solution Initialization. Spatial and temporal finite volume discretizations are specified to be Gaussian linear (central differencing) with upwind vector bias (second order) given to velocity computations. A fully bounded limitation is imposed on all pressure field computations to improve solution stability. Pressure and velocity solvers are preconditioned with a diagonal-based incomplete cholesky preconditioner.

The flow domain is initialized by applying a fixed zero static pressure outlet condition. Thereafter, the outlet pressure field is set to a *zeroGradient* boundary condition while fixing a reference pressure cell to a value of zero to maintain boundedness of the solution. Solution convergence is deemed achieved once $\Delta p'_{t-s} < 0.5$ Pa and $P'_F < 5$ W, monitored over at least 1000 iterations. These values were chosen as no significant trend was observed when surpassing the iteration limit during initial simulation tests. All values are expressed as area-weighted averages between the inlet and outlet evaluation planes and the relevant surface patches. Final results are averaged over one solution oscillation once no noticeable average trends are observed.

High oscillatory behavior of the solution was found at low flowrates. Consequently, a steady-state solution could not be obtained. As such, a large time-step transient solver (*pimpleFoam*) was used to simulate all lower than DP flowrates as the implicit solver provided for an unconditionally stable solution. The large time-step solver allows simulations with higher than normal courant numbers (*Co*), which results in a decrease in computational time yet has a higher probability of introducing instability and temporal diffusion. Therefore, a *Co* number of 5 is used as a maximum to initially speed up simulation convergence, after which it is reduced depending on the solution stability.

All simulations are run in parallel over 24 Intel® Xeon® CPU cores. A maximum simulation time of 384 h was observed for the time-dependent solution at the lowest evaluated flowrate of 9.29 m^3/s, with an average time-step of 3.3×10^{-6} s. Contrary to this, a maximum simulation time of 48 h was observed for all steady-state solutions.

Table 3 Turbulence model comparison of the scale M-Fan at the 14.68 m^3/s calculated DP flowrate of Wilkinson et al. [2] for a 6 mm tip clearance

Turbulence model	Δp_{t-s} (Pa)	η_{t-s} (−)
$k-\omega$ SST [16]	74.70	0.459
Transitional $k-kl-\omega$ [22]	84.58	0.524
LaunderSharma $k-\epsilon$ [23]	72.89	0.454
Experimental [2]	73.99	0.474

FAN Scaling at Various TIP Clearances

When conducting scale experimental tests, the fan's volumetric flowrate and rotational speed are altered to compensate for a change in impeller diameter. However, when varying the tip clearance during such tests, the casing diameter of the test facility remains fixed while the blade tip diameter is altered to achieve the desired tip clearance. This means that the scaling factor, and hence the scale fan's DP flow rate, changes when varying the tip clearance. Using the fan scaling laws and the experimental test facility's casing diameter (measured to be 1.542 m at Stellenbosch University's fan test facility), the theoretical DP specifications of the scale M-Fan at various tip clearances are given in Table 4.

Validation of Results

Validation is performed by assessing the numerical results in terms of its variation and bias against the experimental data. Figure 3 compares the experimental and numerical performance characteristics of the various tip clearance cases.

Variation. As presented in Table 5, due to the experimental data likely consisting of error and uncertainty, the root-mean-square deviation (RMSD) of the numerical results are compared to the maximum experimental test facility's standard deviation. As evident, only the Δp_{t-s} and η_{t-s} of the 6 mm numerical results lie within this limit. This could be due to the mesh convergence study being performed using a 6 mm tip clearance. It would have been more correct to have used the smaller 2 mm tip clearance; yet this would have meant an overall increase in the mesh cell count for all subsequent meshes and thus a further increase in computational time. However, as the current design is intended to improve the M-Fan's performance at the design tip clearance (equivalent scale being 6 mm), the smaller tip clearances are only

Table 4 Scale M-Fan calculated DP specifications for various tip clearance

Tip clearance	D_F (m)	$\dot{V}$ (m^3/s)
2 mm	1.538	14.80
4 mm	1.534	14.68
6 mm	1.530	14.57

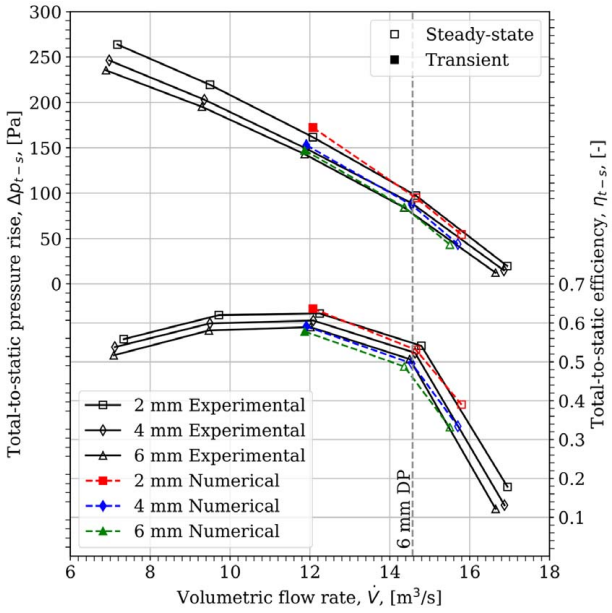

Fig. 3 Scale M-Fan numerical and experimental [2] total-to-static pressure rise and efficiency characteristic curves at various tip clearances

Table 5 Comparison of numerical RMSD and maximum experimental test facility standard deviation of the scale M-Fan at various tip clearances

	RMSD		
Tip clearance	Δp_{t-s} (Pa)	P (W)	η_{t-s} (–)
2 mm	6.678	220.31	0.0142
4 mm	5.255	171.22	0.0194
6 mm	3.772	129.61	0.0152
Experimental σ_{max} [2]	5.221	28.45	0.0385

used for comparative purposes and the results are therefore deemed sufficient.

Bias. To determine the bias of the numerical results, a comparison is made between the differences in experimental and numerical data to that found in the literature (shown in Table 6). As evident, the differences are comparable to that found in former studies conducted on industrial axial flow fans. This demonstrates the validity in using the proposed meshing strategy and numerical setup for modeling the M-Fan.

Effect of TIP Clearance on FAN Performance

Vortex Visualization. Normalized helicity H_{norm} contours are used in the visualization and quantification of the vortex core

Table 6 Difference in experimental and numerical results of the scale M-Fan compared to the literature evaluated at each fan's respective DP flowrate

		Variable	
Fan	τ	$\Delta p_{n/e}$ (Pa)	$\Delta \eta_{n/e}$ (–)
Scale M-Fan (this study)	4.0 mm	0.57	0.024
Scale M-Fan [2]	4.0 mm	3.77	0.012
AC90/6 [9–11]	3.5 mm	1.50	0.020

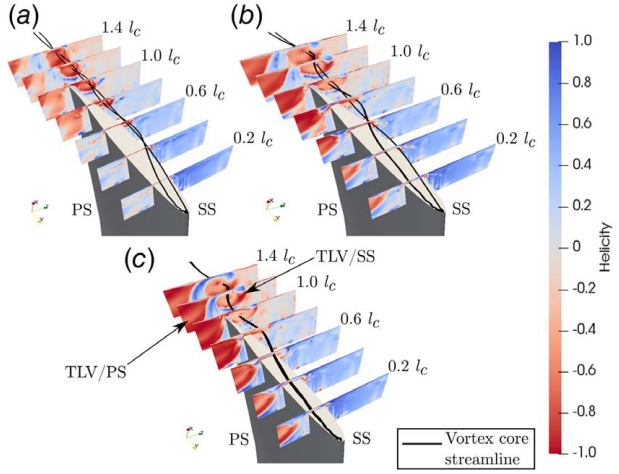

Fig. 4 Normalized helicity H_{norm} cross-sectional contours of scale M-Fan at blade tip with suction-side vortex core visualization for various tip clearances at their respective DP flowrate: (*a*) $\tau = 2$ mm, (*b*) $\tau = 4$ mm, and (*c*) $\tau = 6$ mm

near the blade tip. Normalized helicity is defined as follows: $H_{norm} = (\vec{U} \cdot \vec{v})/|\vec{U}||\vec{v}|$, where $\vec{U}$ is the absolute velocity vector, $\vec{v}$ is the absolute vorticity vector, and $|\vec{U}|$ and $|\vec{v}|$ are their respective magnitudes. This value indicates the orientation of the velocity vector with respect to the vorticity vector. This is used to determine the presence of a vortex core as both vectors tend to align themselves parallel within the core thereby tending to the outer limits of the given range (that being either −1 or 1).

Figure 4 compares cross-sectional contours of the normalized helicity distributions at the blade tip for various tip clearances of the scale M-Fan at their respective DP flowrates (details given in Table 4). Vortex core streamlines are identified based on minimum H_{norm} value as this value was identified to be synonymous with the location of the vortex core. All three cases suggest the presence of a primary clockwise rotating vortex structure located on the blade's suction side (denoted TLV/SS). All vortex cores originate between 0.2 and 0.4 chord fractions, which agrees well with the findings in the literature [8,11]. When examining the contours on the blade's pressure side, the existence of a secondary clockwise rotating vortex structure (denoted TLV/PS) becomes evident. The size of both vortex structures increases with an increase in tip clearance.

Figure 5 visualizes the vortex development within the tip region over one blade pitch. As illustrated, the TLV/SS moves downstream and extends from the forward blade toward the path of the next blade, thereby becoming the secondary vortex structure TLV/PS. These two vortex structures then interact along the blade's chord and merge further downstream, forming a larger vortex structure. The merging of these two vortex structures has been described to affect the blade-to-blade flow field [12].

Vortex Quantification. Figure 6 gives a comparison of the relative TLF velocity, W_{TLF}, and TLV/SS exit trajectory angle, β_{TLV}, along the blade's chord for the scale M-Fan at various tip

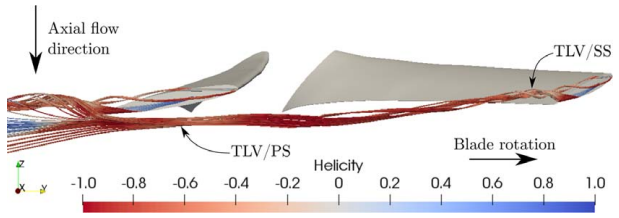

Fig. 5 Blade-to-blade tip leakage vortex interaction

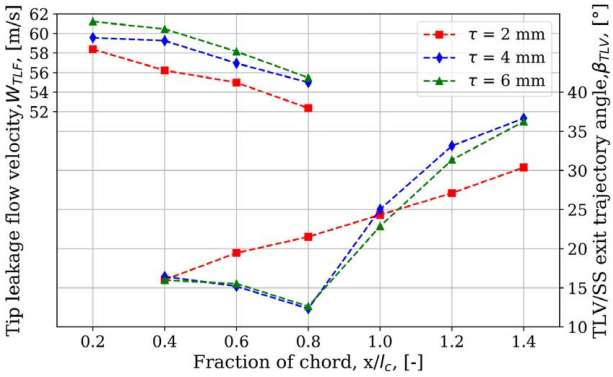

Fig. 6 Relative tip leakage flow velocity and suction-side vortex exit trajectory angle of scale M-Fan at various tip clearances

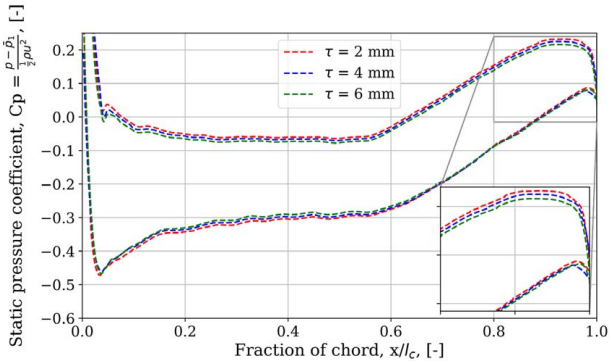

Fig. 7 Chord-wise static pressure coefficient distributions *Cp* of scale M-Fan at various tip clearances evaluated at 0.94r_F

clearances. The W_{TLF} value is averaged across the tip gap, while the β_{TLV} angle is measured relative to the blade's chord for each respective chord-wise *abscissae*.

Reducing the tip clearance has the effect of reducing the relative TLF velocity within the tip gap along the blade's chord. This finding agrees with that found by Venter and Kröger [17] who suggests that the reduction in the TLF velocity within the tip gap, as a result of a reduction in the tip clearance, owes to a reduction in the associated pressure losses. A reduction in the relative TLF velocity would additionally have a beneficial effect on the momentum transfer to the TLV/SS, thereby reducing both its size and intensity.

Comparing the TLV/SS exit trajectory angles of the various cases, both the 4 mm and 6 mm cases follow a similar decreasing exit angle trend along the blade's chord, whereas the 2 mm case has the opposite effect. This could be a result of the interaction between the developing vortex core and the suction-side pressure field. As previously noted, an increase in the size of each vortex structure is evident with an increase in tip clearance. The larger the vortex on the blade suction side, the further it will extend in the spanwise direction meaning it will be more influenced by the blade's suction-side pressure field. This would cause the vortex to be "drawn" closer to the blade surface, which would explain the initial decrease in exit trajectory angle of the 4 mm and 6 mm cases.

When evaluating the TLV/SS exit trajectory angles beyond the blades trailing edge, it is evident that a reduction in the tip clearance is characterized by an overall reduction in the TLV/SS exit trajectory angle. This would be synonymous with a reduction in the size of the TLV as a diminished vortex would experience an overall reduced effect from the spanwise pressure field.

Studying the effect of the TLV/SS on the formation of the TLV/PS, a direct interdependence is found to exist between the two flow phenomena. The greater interaction and subsequent merging of these two vortex structures could be attributed to the increased exit trajectory angle and increased relative TLF velocity of the larger tip clearance cases.

Blade Surface Pressure Analysis. Blade surface pressure distributions, *Cp*, are considered for describing the interaction between the TLV and near-surface flow field near the blade tip. The static pressure coefficient is defined as follows: $Cp = (p - \bar{p}_1)/\frac{1}{2}\rho u^2$, where $\bar{p}_1$ represents the average static pressure evaluated at the inlet of the domain and u represents the blade's tangential velocity component evaluated at a constant radius. The location of the evaluation surface is chosen such that the TLV core remains intact.

The static pressure distributions illustrated in Fig. 7 give evidence to an improved pressure field distribution near the blade tip with a reduction in tip clearance. These findings concur with that found by Cumpsty and Storer [18]. This would correspond to an improved surface flow field due to a reduced effect from the created vortex structure interaction.

When examining the suction-side pressure field distributions, a consistent distribution is apparent after roughly 0.6 chord fractions for all tip clearance cases. This suggests that the suction-side pressure distributions near the trailing edge of the blade tip are less affected by a reduction in tip clearance. A possible explanation for this could be due to the spanwise TLV development interacting with the suction-side surface flow field.

Aerodynamic Performance Analysis. Referring back to Fig. 3 and comparing fan performance characteristics between the various tip clearance cases, a near linear increase in all performance metrics across the fan's entire stable operating range becomes evident with a reduction in tip clearance. These findings are in agreement with that found by Venter and Kröger [17]. This suggests that minimizing the tip clearance reduces the effect of the TLF, thereby reducing the associated pressure losses.

Table 7 summarizes the experimental and numerical results of each tip clearance at its respective DP flowrate. Analyzing the results indicates an improved performance of 15.6% in the total-to-static pressure rise and a 5.1% point increase in total-to-static efficiency with a 66.6% reduction in tip clearance. The subsequent sections describe the investigation into this mechanism further.

TIP Appendage Design

Two predominant TLF characteristics are evident with a reduction in tip clearance, these being a decrease in the relative TLF velocity within the tip gap and a decrease in the TLV exit trajectory angle along the blade's chord. From the aerodynamic performance analysis, the reduction of such flow characteristics is associated with having a beneficial effect on fan performance characteristics. The following sections investigate the design for control of these two flow characteristics for the scale M-Fan (details given in Table 1 and henceforth referred to as the fan *datum*).

Tip Leakage Flow Velocity Control. Corsini and Sheard [9] found, through experimental testing, an improvement in fan static efficiency by up to 2.0% points at the fan's DP flowrate with the

Table 7 Scale M-Fan DP performance characteristics at various tip clearances

	Experimental		Numerical	
Tip clearance	Δp_{t-s} (Pa)	η_{t-s} (–)	Δp_{t-s} (Pa)	η_{t-s} (–)
2 mm	92.48	0.540	89.81	0.518
4 mm	84.67	0.514	81.96	0.481
6 mm	77.58	0.494	77.72	0.467

addition of a constant thickness (CT) end-plate tip appendage (note that some authors refer to width instead of thickness). This was achieved by locally thickening the blade tip on the blade's pressure side by a factor of three with respect to the maximum blade tip thickness. This dimension was chosen according to a reference radial dimension for control of the TLV. The introduction of such an end-plate was found to control the TLF by reducing its relative velocity component within the tip gap [11]. This thickness ratio of 3:1 is taken as the upper limit of the current end-plate design.

As described by Denton [19], if the tip clearance is less than 25% of the blade's thickness, a subsequent mixing of the TLF will occur with an increase in the static pressure and entropy across the tip gap. This mixing may hinder the TLF, thereby resulting in its diminution. As a result, this thickness is considered as the lower limit for the end-plate design.

The thickness limits for the proposed CT end-plate design are summarized as follows:

$$t_{ep} = \begin{cases} 3\max(t_{blade}), & \text{maximum} \\ 4\tau, & \text{minimum} \end{cases} \quad (1)$$

Corsini et al. [9–12] only consider the effect of an end-plate on the blade's pressure side, yet, and Cumpsty and Storer [18] propose that it is the blade's suction side that is responsible for controlling the chord-wise TLF distribution. Consequently, this article conducts an investigation involving a CT end-plate on both the blade pressure side and suction side to evaluate its effect on fan performance.

The blade tip is locally thickened, from blade chord, using the given criteria as set out in Eq. (1). Figure 8 illustrates the final CT end-plate designs, denoted CT/PS/24, CT/PS/47, and CT/SS/24, with the unmodified datum blade for comparison. The corresponding minimum and maximum end-plate thicknesses for the fan datum are 24 mm and 47 mm, respectively. The end-plates are extruded at a constant radius to maintain a constant tip gap.

Vortex analysis. Vortex visualization and quantification of the CT end-plate designs are illustrated in Figs. 9 and 10, respectively. All three designs show the same presence of two clockwise rotating vortex structures, that being TLV/PS and TLV/SS, as seen previously in the datum fan case. Comparing the helicity contour plots

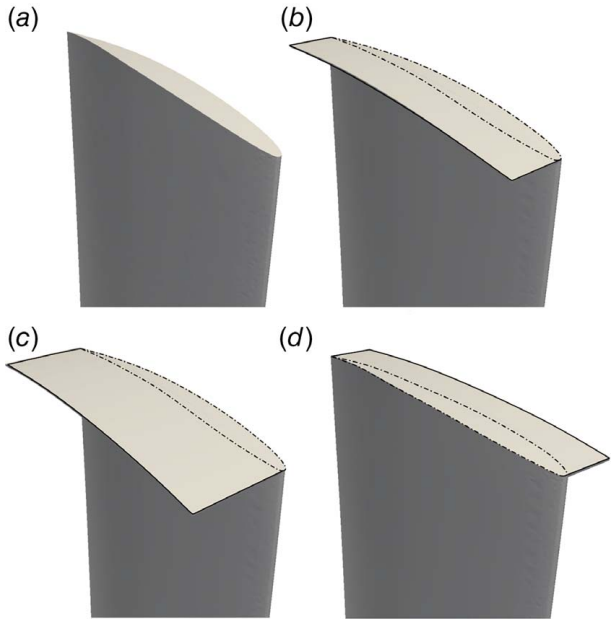

Fig. 8 Fan datum and CT end-plate designs: (*a*) datum, (*b*) 24 mm pressure-side end-plate, (c) 47 mm pressure-side end-plate, and (*d*) 24 mm suction-side end-plate

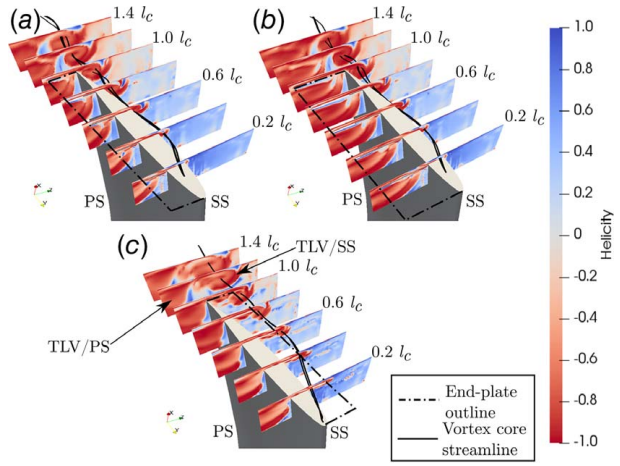

Fig. 9 Normalized helicity H_{norm} cross-sectional contours at blade tip with suction-side vortex core visualization with a 6 mm tip clearance at the fan's 14.57 m^3/s DP flowrate: (*a*) CT/PS/24, (*b*) CT/PS/47, and (*c*) CT/SS/24

of the pressure-side end-plate designs (Fig. 9) with that of the datum fan (Fig. 4(*c*)), no noticeable difference is found in terms of the vortex's size or intensity.

An overall reduction in the relative TLF velocity within the tip gap is observed for all CT end-plate designs when compared to the fan datum (Fig. 10), with an average reduction of 6.8% for the CT/PS/47 and CT/SS/24 end-plate designs. Evaluating the TLV/SS exit trajectory angles between the various designs, both CT/PS end-plate designs are found to reduce the TLV/SS exit trajectory angle beyond the trailing edge of the blade, with a further reduction as the end-plate thickness is increased.

A significant increase in the TLV/SS exit trajectory angle is evident with the introduction of the CT/SS/24 end-plate design. This is due to the suction-side end-plate design extending the vortex's inception point further away from the blade's surface, thereby forcing it to have a larger exit trajectory angle. This causes the vortex to become more elongated and elliptical in shape while also increasing its size when compared to the datum.

Blade surface pressure analysis. Examining the various surface pressure distributions toward the blade's trailing edge (Fig. 11), a decrease in blade loading is evident through the addition of all CT end-plate designs when compared to the fan datum. A reduction in blade loading suggests a reduction in fan performance characteristics as the tip region is consequently more affected by the TLV. These findings suggest that an aft-loaded blade is desirable when

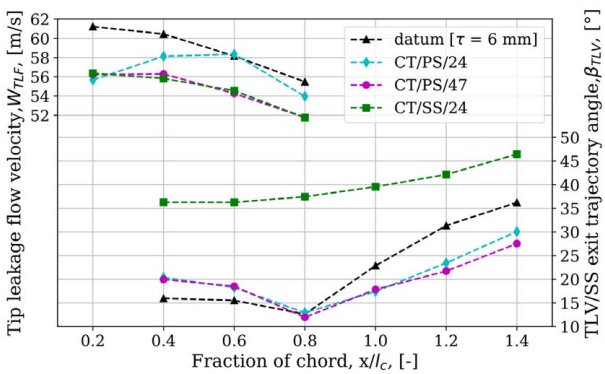

Fig. 10 Relative tip leakage flow velocity and suction-side vortex exit trajectory angle of fan datum and CT end-plate designs evaluated at the fan's 14.57 m^3/s DP flowrate

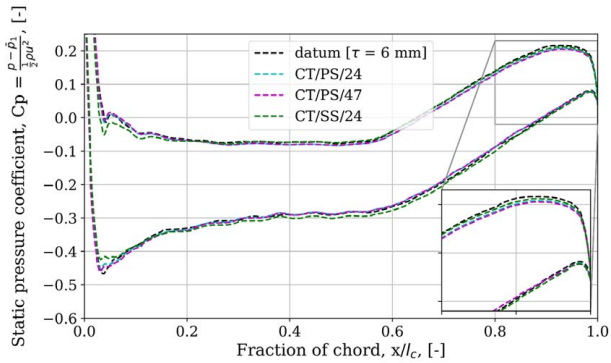

Fig. 11 Chord-wise static pressure coefficient distributions *Cp* of fan datum and CT end-plate designs evaluated at 0.94r_F

optimizing blade loading distributions for fan performance enhancement. Supporting literature is found to concur with the former when considering loss generation associated with compressor stage performance, which finds delayed TLV formation with a reduced mixed-out TLF at the outlet [20].

Aerodynamic performance analysis. Analyzing the CT end-plates' characteristic curves (Fig. 12), improved performance for all pressure-side CT end-plate designs at below DP flowrates is achieved with increasing performance toward the rotor stall margin. These findings concur with that found by Corsini et al. [10] who made use of a similar end-plate design. The results of the suction-side CT end-plate design indicate maintained or otherwise reduced performance characteristics. It is for this reason that no further CT/SS end-plate designs were tested.

None of the CT end-plate designs are found to improve the fan's performance at the DP flowrate (Table 8). A possible explanation for this could be due to the CT end-plate design being less effective in controlling the TLV/SS at relatively higher flowrates. At these operating conditions, a smaller vortex would be created due to a lower blade loading, coupled with higher flow velocities evoking greater viscous losses with the addition of the end-plates additional surface area. All these factors contribute to a reduced design effectiveness. Supporting evidence, previously visualized in the helicity

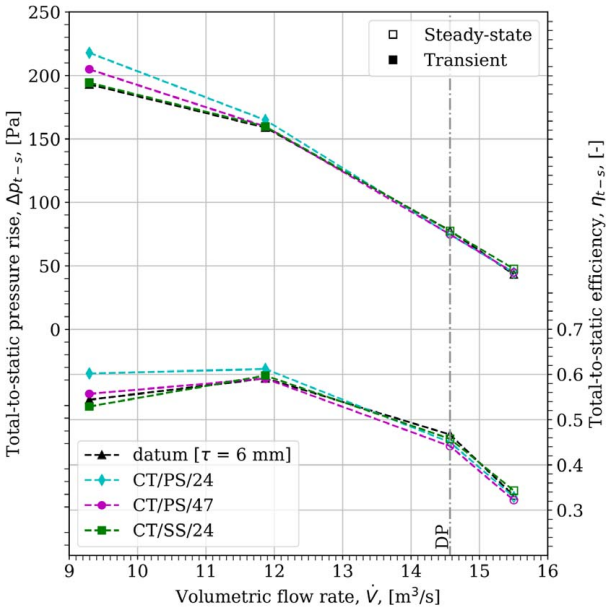

Fig. 12 Numerical total-to-static pressure rise and efficiency characteristic curves of fan datum and CT end-plate designs

Table 8 Numerical fan datum and CT end-plates 14.57 m³/s DP performance characteristics

Design	Δp_{t-s} (Pa)	η_{t-s} (–)
datum ($\tau = 6$ mm)	77.72	0.467
CT/PS/24	74.66	0.450
CT/PS/47	74.81	0.441
CT/SS/24	77.41	0.458

contour plots (Fig. 9), shows no reduction in the vortex's size or intensity when compared to the fan datum. These findings suggest the CT end-plate design to have a specific beneficial operating range, whereby effective control of the TLV can be implemented.

A consistent reduction in fan performance characteristics is observed when increasing the pressure-side CT end-plate's thickness from 24 mm to 47 mm. This suggests that an operating point-specific end-plate thickness exists to control the TLV, while minimizing the induced losses associated with the design's introduced surface area.

Tip Leakage Vortex Exit Trajectory Control. A reduction in the tip clearance correlates with a decrease in the TLV/SS exit trajectory angle. Discovered during the datum fan analysis, the largest TLV/SS exit trajectory gradient is found to occur between 1.0 and 1.2 chord fractions. Extension of the TE of the datum fan within this region through the use of an end-plate design could provide for the reduction and subsequent control of the TLV/SS exit trajectory angle. The novel end-plate concept would extend in the spanwise direction and cover the size of the vortex to be controlled. An additional benefit of the TE end-plate design is the creation of a localized aft pressure differential near the blade tip as a result of the pressure-side flow deflection. This in turn should shift the blade's peak loading distribution further aft toward the blade's trailing edge, which has been described to have a beneficial effect on compressor stage loss generation [20].

The end-plate dimension requirements for the proposed TE end-plate design are summarized in Eq. (2).

$$h_{ep} = 0.03 D_F \qquad l_{ep} = 0.2 l_c \tag{2}$$

Figure 13 illustrates the TE end-plate design. The end-plates are extruded, such that a constant tip clearance is maintained. The angle ζ_{ep} is defined as the setting angle of the end-plate relative to the blade chord. As the setting angle is increased from a zero angle, the end-plate will increasingly deflect the pressure-side flow, thereby deflecting the TLV/PS further in the axial direction. Consequently, this will affect the TLV/SS exit trajectory angle, which will reduce the vortex–vortex interaction.

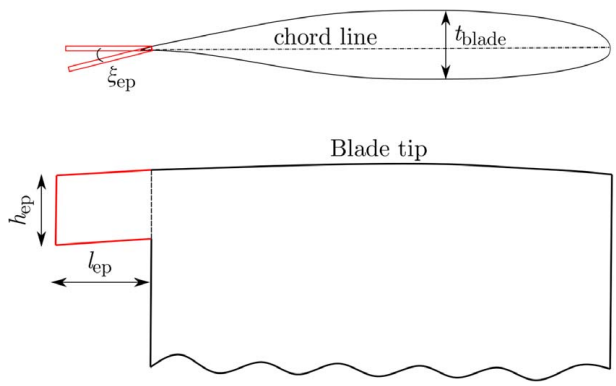

Fig. 13 TE end-plate design

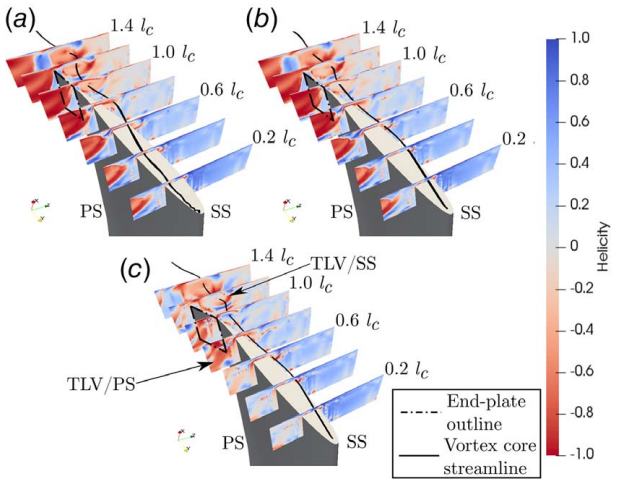

Fig. 14 Normalized helicity H_{norm} cross-sectional contours at blade tip with the suction-side vortex core visualization with a 6-mm tip clearance at the fan's DP flowrate: (*a*) TE/PS/0 deg, (*b*) TE/PS/4 deg, and (*c*) TE/PS/15 deg

A range of end-plate setting angles for the proposed TE end-plate design is chosen based on the flat plate theory to reduce the inherent complexity of the tip flow interaction. This is to acquire an initial range of values to determine design feasibility. End-plate setting angles are determined through use of experimental lift (C_L) and mid-chord moment coefficients ($C_{M,mc}$) for a flat plate of similar size to that of the proposed design and at a similar Reynolds number to the design's intended operating point [21]. Three end-plate setting angles are chosen for evaluation; that being 0 deg, 4 deg, and 15 deg, as these provide for a sufficient compromise between maximizing the C_L value while minimizing the exerted moment force. The final TE end-plate designs are denoted TE/PS/0 deg, TE/PS/4 deg, and TE/PS/15 deg.

Vortex analysis. Considering the helicity contour plots (Fig. 14), a noticeable reduction in the size and intensity of the TLV/PS structure is apparent with an increase in the TE end-plate's setting angle. This reduction is comparable to that experienced with a reduction in tip clearance. Likewise with the 2-mm tip clearance datum case, the TLV/PS is almost unrecognizable in the TE/PS/15 deg case. This suggests that the TE end-plate design has a beneficial effect on the TLV/SS, consequently reducing the interaction between the two vortex structures TLV/SS and TLV/PS.

Quantification of the vortex metrics (Fig. 15) confirm a reduction in the TLV/SS exit trajectory angle with an increase in the TE end-plate setting angle. An increase in the TLF within the tip gap is also

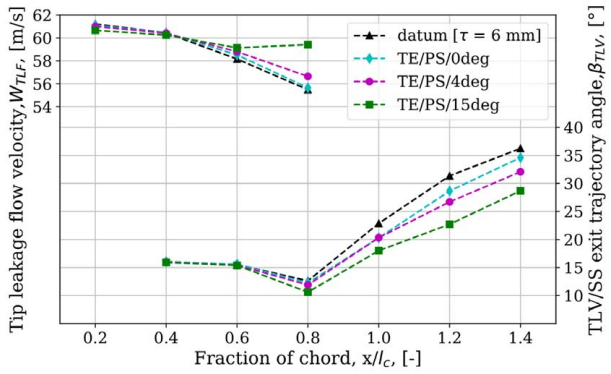

Fig. 15 Relative tip leakage flow velocity and suction-side vortex exit trajectory angle of fan datum and TE end-plate designs evaluated at the fan's 14.57 m^3/s DP flowrate

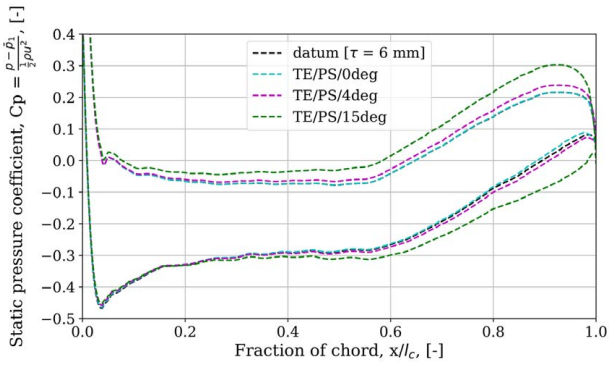

Fig. 16 Chord-wise static pressure coefficient distributions *Cp* of fan datum and TE end-plate designs evaluated at 0.94r_F

evident with an increase in the end-plate setting angle. Contrary to this, the TLF is thought to be one of the predominant driving mechanisms behind the formation of the TLV, and its reduction is desirable when considering loss generation.

Blade surface pressure analysis. Evaluating the surface pressure distributions of the various TE end-plate designs (Fig. 16), an increase in blade loading toward the aft section of the blade tip is clear. As previously explained, this is associated with improved loss behavior and delayed TLV formation [20]. This effect additionally accounts for the increased relative TLF within the tip gap, previously associated with the introduction of the TE end-plate design. This would attest to the blade tip loading distribution being more crucial in reducing the associated TLV losses than the relative TLF velocity at higher than peak efficiency flowrates.

Aerodynamic performance analysis. Evaluating the aerodynamic performance characteristic curves of the various TE end-plate designs (Fig. 17), the upper and lower bounds of the end-plate setting angles achieve an increase in fan performance characteristics in different regions of the fan's operation. This is a consequence of a lower blade loading being present at higher flowrates, which necessitates a greater TLV/SS deflection and hence, equivalently, a higher end-plate setting angle. However, the higher end-plate

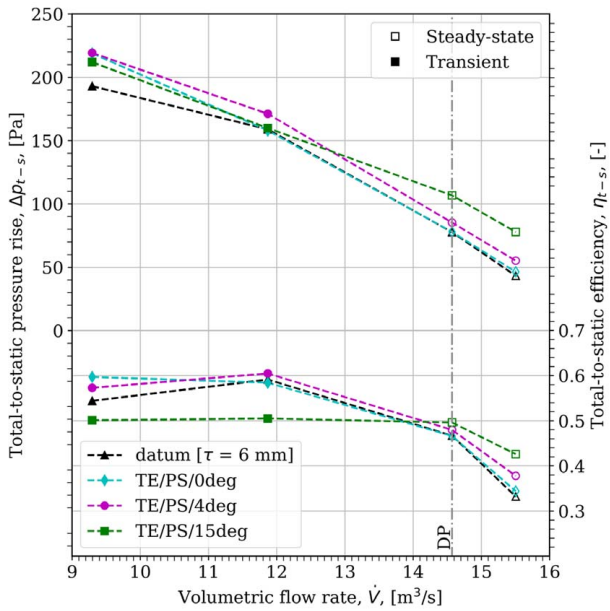

Fig. 17 Numerical total-to-static pressure rise and efficiency characteristic curves of fan datum and TE end-plate designs

Table 9 Numerical fan datum and TE end-plates 14.57 m^3/s DP performance characteristics

Design	Δp_{t-s} (Pa)	η_{t-s} (–)
Datum ($\tau = 6$ mm)	77.72	0.467
TE/PS/0 deg	77.89	0.466
TE/PS/4 deg	85.29	0.480
TE/PS/15 deg	106.73	0.496

setting angle provides for the reduced performance at lower flowrates due to the increased flow separation. These findings suggest that an operating point-specific end-plate setting angle exists, whereby effective control of the TLV/SS exit trajectory angle can be implemented. This also attests to the adequacy of the chosen TE end-plate setting angle range for describing the performance bounds of the design. The TE/PS/0 deg and TE/PS/4 deg end-plate designs indicate an improved rotor stall margin efficiency plateau, as evident in the CT end-plate designs. Overall, the TE/PS/4 deg end-plate design is found to provide an intermediate between the two design extremes, achieving improved performance characteristics over the entire evaluated stable operating range.

Considering the aerodynamic performance characteristics at the fan's DP flowrate (Table 9), improved or otherwise maintained performance is evident for all end-plate designs. The TE/PS/15 deg end-plate design offers a superior performance improvement when compared to the other designs, with an indicated increase of 37.3% in total-to-static pressure rise and a 2.9% point increase in the total-to-static efficiency.

Conclusions

The present study conducts numerical investigations into tip clearance effects specific to axial flow fan performance characteristics. The aim of this study is to gain understanding into the relevant leakage flow phenomena present near the blade tip to implement a tip appendage design for their control and subsequent enhancement of fan performance characteristics.

A periodic three-dimensional model is developed using a novel open-source meshing strategy. The results indicate good correlation with the experimental data, and the differences are comparable to those found in literature. Helicity contour plots of the blade tip region are introduced to visualize and quantify the effect of the TLV when varying the tip clearance. The findings, along with relevant literature, are used to identify two predominant leakage flow phenomena for control, namely, (i) the relative TLF velocity within the tip gap and (ii) the TLV exit trajectory angle relative to the blade chord. Finally, two design strategies are implemented to mitigate the detrimental effects of the identified flow phenomena and to determine their effect on the fan's performance characteristics.

The introduction of three CT end-plate design concepts is provided for the control of the relative TLF velocity within the tip gap. Aerodynamic performance results indicate improved performance characteristics at below design point flowrates with an increased efficiency plateau toward the rotor stall margin. This low flow performance boost is rather significant given the fans application in ACHEs where off design conditions are often encountered. The findings suggest that an operating point-specific CT end-plate thickness exists, whereby effective control of the TLV can be implemented over a specific beneficial operating range.

Through introduction of a novel trailing-edge (TE) end-plate design, the mitigation of the TLV exit trajectory angle is implemented. The end-plate design achieved control of the TLV exit trajectory angle through its reduction, which consequently reduced the blade-to-blade vortex interaction. The aerodynamic performance results indicate improved fan performance characteristics across the entire evaluated stable operating range, with a specific end-plate setting angle being better suited for specific operating conditions. This attests to the effectiveness of the TE end-plate design in controlling the TLV exit trajectory angle and that an optimal operating point-specific end-plate setting angle exists. Future contributions will include the optimization and experimental validation of the design as well as a more detailed analysis into the controlling loss mechanisms.

Acknowledgment

The present research received funding from the European Union's Horizon 2020 research and innovation program (Grant No. 654443). Financial assistance from the Hillensberg trust and Stellenbosch University is also acknowledged.

Conflict of Interest

There are no conflicts of interest.

Data Availability Statement

The datasets generated and supporting the findings of this article are obtainable from the corresponding author upon reasonable request. The authors attest that all data for this study are included in the paper. Data provided by a third party listed in Acknowledgment.

Nomenclature

h = height
t = thickness
r = radius
D = diameter
W = relative velocity
l_c = blade chord length
Cp = static pressure coefficient
H_{norm} = normalized helicity
P, p = power, static pressure, respectively
U, u = absolute and blade tangential velocities, respectively
$\dot{V}$, v = volume flowrate, absolute vorticity, respectively
β = exit trajectory angle
ζ = setting angle
η = efficiency
ρ = air density
τ = tip clearance

Subscripts

ep = end-plate
F = fan
n/e = numerical versus experimental
$t-s$ = total to static
1 = static inlet location

Superscripts

$\bar{}$ = average quantity
$'$ = fluctuating quantity

References

[1] Wilkinson, M. B, 2017, "The Design of an Axial Flow Fan for Air-Cooled Heat Exchanger Applications," M.S. thesis, Stellenbosch University, Stellenbosch, WC.
[2] Wilkinson, M. B., van der Spuy, S. J., and von Backström, T. W., 2019, "Performance Testing of an Axial Flow Fan Designed for Air-Cooled Heat Exchanger Applications," ASME J. Eng. Gas. Turbines. Power., **141**(5), p. V001T09A005.
[3] Cumpsty, N. A., 2004, *Compressor Aerodynamics*, Krieger Publishing Company, Malabar.

[4] Mitchell, A. M., and Delery, J., 2001, "Research Into Vortex Breakdown Control," Progress Aeros. Sci., **37**(4), pp. 385–418.
[5] Vad, J., 2008, "Aerodynamic Effects of Blade Sweep and Skew in Low-Speed Axial Flow Rotors at the Design Flow Rate: An Overview," Proc. Insti. Mech. Eng., Part A J. Power Energy, **222**(1), pp. 69–85.
[6] Ye, X., Li, P., Li, C., and Ding, X., 2015, "Numerical Investigation of Blade Tip Grooving Effect on Performance and Dynamics of an Axial Flow Fan," Energy, **82**, pp. 556–569.
[7] Jiang, D., Luo, H., and Zhang, X., 2015, "Numerical Study of the Leakage Flow on a Novel Turbine Blade Tip," Procedia. Eng., **99**, pp. 413–422.
[8] Ye, X., Zhang, J., and Li, C., 2017, "Effect of Blade Tip Pattern on Performance of a Twin-Stage Variable-Pitch Axial Fan," Energy, **126**, pp. 535–563.
[9] Corsini, A., and Sheard, A. G., 2007, "Tip End-Plate Concept Based on Leakage Vortex Rotation Number Control," J. Comput. Appl. Mech., **8**(1), pp. 21–37.
[10] Corsini, A., Rispoli, F., and Sheard, A. G., 2007, "Development of Improved Blade Tip End-Plate Concepts for Low-Noise Operation in Industrial Fans," Proc. Insti. Mech. Eng., Part A J. Power Energy, **221**(5), pp. 669–681.
[11] Corsini, A., Rispoli, F., and Sheard, A., 2010, "Shaping of Tip End-Plate to Control Leakage Vortex Swirl in Axial Flow Fans," ASME J. Turbomach., **132**(3), p. 031005.
[12] Corsini, A., and Sheard, A. G., 2013, "End-Plate for Noise-by-Flow Control in Axial Fans," Periodica Polytech. Mech. Eng., **57**(2), pp. 3–16.
[13] Louw, F. G, 2015, "Investigation of the Flow Field in the Vicinity of an Axial Flow Fan During Low Flow Rates," Ph.D. thesis, Stellenbosch University, Stellenbosch, WC.
[14] OpenCFD Ltd, 2018, "OpenFOAM User Guide," https://www.openfoam.com/documentation/user-guide/index.php, Accessed June 12, 2018.
[15] Inoue, M., and Furukawa, M., 2002, "Physics of Tip Clearance Flow in Turbomachinery," ASME 2002 Joint US-European Fluids Engineering Division Conference, Montreal, Quebec, United States, July 14.
[16] Menter, F., Kuntz, M., and Langtry, R., 2003, "Ten Years of Industrial Experience With the SST Turbulence Model," Heat Mass Trans., **4**(1), pp. 625–632.
[17] Venter, S., and Kröger, D., 1992, "The Effect of Tip Clearance on the Performance of an Axial Flow Fan," Energy. Convers. Manage., **33**(2), pp. 89–97.
[18] Cumpsty, N. A., and Storer, J. A., 1991, "Tip Leakage Flow in Axial Compressors," ASME J. Turbomach., **113**(2), pp. 252–259.
[19] Denton, J. D., 1993, "Loss Mechanisms in Turbomachines," ASME Int. Gas Turbine Aeroengine Congress Exposition, **115**(4), pp. 19–21.
[20] Tiralap, A., Tan, C. S., Donahoo, E., Montgomery, M., and Cornelius, C., 2017, "Effects of Rotor Tip Blade Loading Variation on Compressor Stage Performance," ASME J. Turbomach., **139**(5), p. 051006.
[21] Amandolese, X., Michelin, S., and Choquel, M., 2013, "Low Speed Flutter and Limit Cycle Oscillations of a Two-Degree-of-Freedom Flat Plate in a Wind Tunnel," J. Fluids Struct., **43**, pp. 244–255.
[22] Walters, D. K., and Cokljat, D., 2008, "A Three-Equation Eddy-Viscosity Model for Reynolds-Averaged Navier-Stokes Simulations of Transitional Flow," J. Fluid. Eng., **130**(12), p. 121401.
[23] Launder, B., and Spalding, D., 1974, "The Numerical Computation of Turbulent Flows," Comput. Methods Appl.Mech. Eng., **3**(2), pp. 269–289.